Inference of Black Hole Fluid-Dynamics from Sparse Interferometric Measurements: Supplementary Material

Aviad Levis[1*], Daeyoung Lee[2], Joel A. Tropp[1], Charles F. Gammie[2], Katherine L. Bouman[1]
[1]California Institute of Technology, [2]University of Illinois
*alevis@caltech.edu

In this accompanying text we provide extended derivations, analysis and results that were excluded from the main text. Note that supplementary sections, equations, and figures are all marked with an "S" prefix.

S1. Astrophysical Accretion Disks as GRFs

In Sec. 2.2 of the main text we describe an approach to efficiently model Gaussian Random Fields (GRF) as a solution to a stocastic partial differential equation (SPDE) [10, 6, 3]. In particular, Sec. 2.2.1 describes the anisotropic spatio-temporal diffusion equation. This SPDE is able to capture the (in homogeneous and non-isotropic) variability of astrophysical accretion disks [5] through a spatially variable diffusion tensor $\mathbf{\Lambda}(\boldsymbol{x})$ (Sec. 2.2.2). In the following we describe the accretion model parameters which dictate the diffusion tensor through the following fields (Eqs. 5–8):

$$\boldsymbol{v}_x(\boldsymbol{x}), \boldsymbol{v}_y(\boldsymbol{x}), \phi(\boldsymbol{x}), \lambda_0(\boldsymbol{x}), \lambda_1(\boldsymbol{x}), \lambda_2(\boldsymbol{x}). \tag{S1}$$

Consider a polar coordinate system on the image plane parameterized by radius, r, azimuth angle, φ, and their corresponding direction vectors, $\hat{\boldsymbol{r}}$ and $\hat{\boldsymbol{\varphi}}$:

$$r = |\boldsymbol{x}|, \qquad \varphi = \arctan(x_2/x_1), \tag{S2}$$

$$\hat{\boldsymbol{r}} = (\cos\varphi, \sin\varphi), \quad \hat{\boldsymbol{\varphi}} = (-\sin\varphi, \cos\varphi) \tag{S3}$$

Keplerian orbital frequency, Ω_{K}, scales with radius as $\Omega_{\mathrm{K}} \propto r^{-3/2}$. We parameterize the velocity field as (Fig. 2)

$$v_x(r,\varphi;\varphi_0) = -\Omega_{\mathrm{K}}(r)\sin(\varphi+\varphi_0) \tag{S4}$$

$$v_y(r,\varphi;\varphi_0) = \Omega_{\mathrm{K}}(r)\cos(\varphi+\varphi_0), \tag{S5}$$

where Ω_{K} and $\varphi+\varphi_0$ are respectively the magnitude and angle of the velocity vector field. The parameter φ_0 defines the *opening angle* of the velocity field with respect to $\hat{\boldsymbol{\varphi}}$. For example, $\varphi_0 = \{0^\circ, 90^\circ, 180^\circ, 270^\circ\}$ describe counter-clockwise (CCW) flow, radial outflow, clockwise (CW) flow, and radial inflow, respectively. Similarly, the direction of the major and minor spatial correlation axis (Eqs. 7–8) are defined by

$$\phi(\varphi;\varphi_1) = \varphi + \varphi_1, \tag{S6}$$

where φ_1 defines the opening angle of $\boldsymbol{\xi}_1$ with respect to $\hat{\boldsymbol{r}}$. Finally, the remaining correlation lengths required to fully parameterize the diffusion tensor are defined by

$$\lambda_0 \propto \Omega_{\mathrm{K}}^{-1}, \quad \lambda_1(r) \propto r, \quad \lambda_2(r) = \epsilon\lambda_1(r). \tag{S7}$$

Here $\epsilon \in [0,1]$ is a fixed ratio which dictates the directionality of spatial correlations (ϵ=1.0 yields isotropic correlations).

S2. RSI and PCA Comparison

In Sec 4.1 we describe the *random subspace iteration* (RSI) algorithm (Alg. 1) utilized to estimate the top modes of the SPDE system. Another approach to recover the top modes, which capture most of the variability in the GRFs, is to

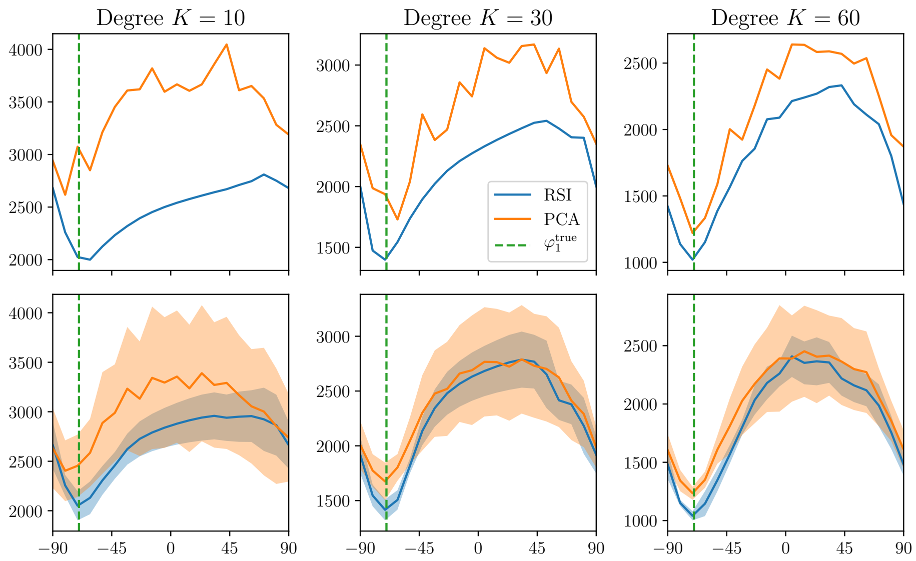

Figure S1: A comparison between RSI (blue) and PCA (orange). RSI modes are computed with q=5 for varying degrees $K = 10, 30, 60$ with the equivalent $50, 150, 300$ PCA samples. The data-fit is plotted for a fixed CW rotation φ_0^{true} and underlying true correlation direction $\varphi_1^{\text{true}} = -70°$ (green). The top row demonstrates the noisy PCA loss of a single measurement instance. Bottom row shows statistics over measurement samples. Much of the variability is not captured by the PCA modes resulting in a higher standard deviation (semi-transparent).

sample many GRFs and use *principle component analysis* (PCA) on the sampled data. For a large number of GRF samples these two approaches converge to the same answer. RSI requires qK forward operations (solving Eq. 1), where q is the number of iterations and K is the degree or block size. For comparison we computed RSI modes with $q = 5$ for varying degrees $K = 10, 30, 60$ with the equivalent $50, 150, 300$ PCA samples, respectively. Figure S1 compares the 1D data-fit $\mathcal{D}(\varphi_0^{\text{true}}, \varphi_1)$ (Sec. 4.2.1) for a fixed CW rotation φ_0^{true} and an unknown spatial correlation direction φ_1. To generate statistics the data-fit was computed for 10 GRF *measurements*, sampled with the underlying true parameters $\varphi_0^{\text{true}}, \varphi_1^{\text{true}}$. The top row demonstrates the noisy loss resulting from PCA for a single measurement instance. Optimizing over the PCA-based loss using gradients would be very challenging due to its rough discontinuous behavior, whereas for the same number of operations RSI results in a much smoother loss. The bottom row shows statistics over 10 measurement samples.

S3. Fitting Accretion Disk Parameters

In the main text we analyze two-dimensional (2D) data-fit manifolds (defined by Eq. 18) for four different dynamic evolutions (Fig. 4) . In Fig. S2 we extend this analysis to a 5×5 grid of measurements; each measurement was synthesized from a different set of accretion parameters $\mathbf{\Theta}_{\text{true}} = (\varphi_0^{\text{true}}, \varphi_1^{\text{true}})$. The inferred global minima track the ground-truth. From Fig. S2 we see that some regions of the parameter space have a wider local minima as visualized by a wider navy colored region. This implies that estimation of these parameters is associated with higher uncertainty. Note that due to periodicity the manifolds wrap around in both the horizontal and vertical axes.

S4. Comparison of Stochastic Model Fitting and Imaging

In the main text we compare our recovery results to a state-of-the-art VLBI imaging approach, *StarWarps* (SW) [1], which was developed to handle time-varying interferometric datasets. The output of SW is an estimated full length video, V^{SW}, from which we extract the mean OpticalFlow (OF) field [2] to approximate the underlying velocity field. Figure S3 shows further comparisons for two underlying true dynamic evolutions generated with $\mathbf{\Theta}_1^{\text{true}}, \mathbf{\Theta}_2^{\text{true}}$. Here $\mathbf{\Theta}_1^{\text{true}}$ denotes CW rotation and $\mathbf{\Theta}_2^{\text{true}}$ denotes radial outflow. Figure S3 demonstrate results for both EHT++ and EHT2017 measurements. The SW motion field, extracted from EHT++ measurements, is able to capture the general direction of the flow (i.e. CW rotation or radial outflow). This suggests that in regimes of dense measurements, imaging as an initial step could be useful for extracting some evolution dynamics. In contrast, Fig. S3 highlights the advantage of having a dynamic model, especially

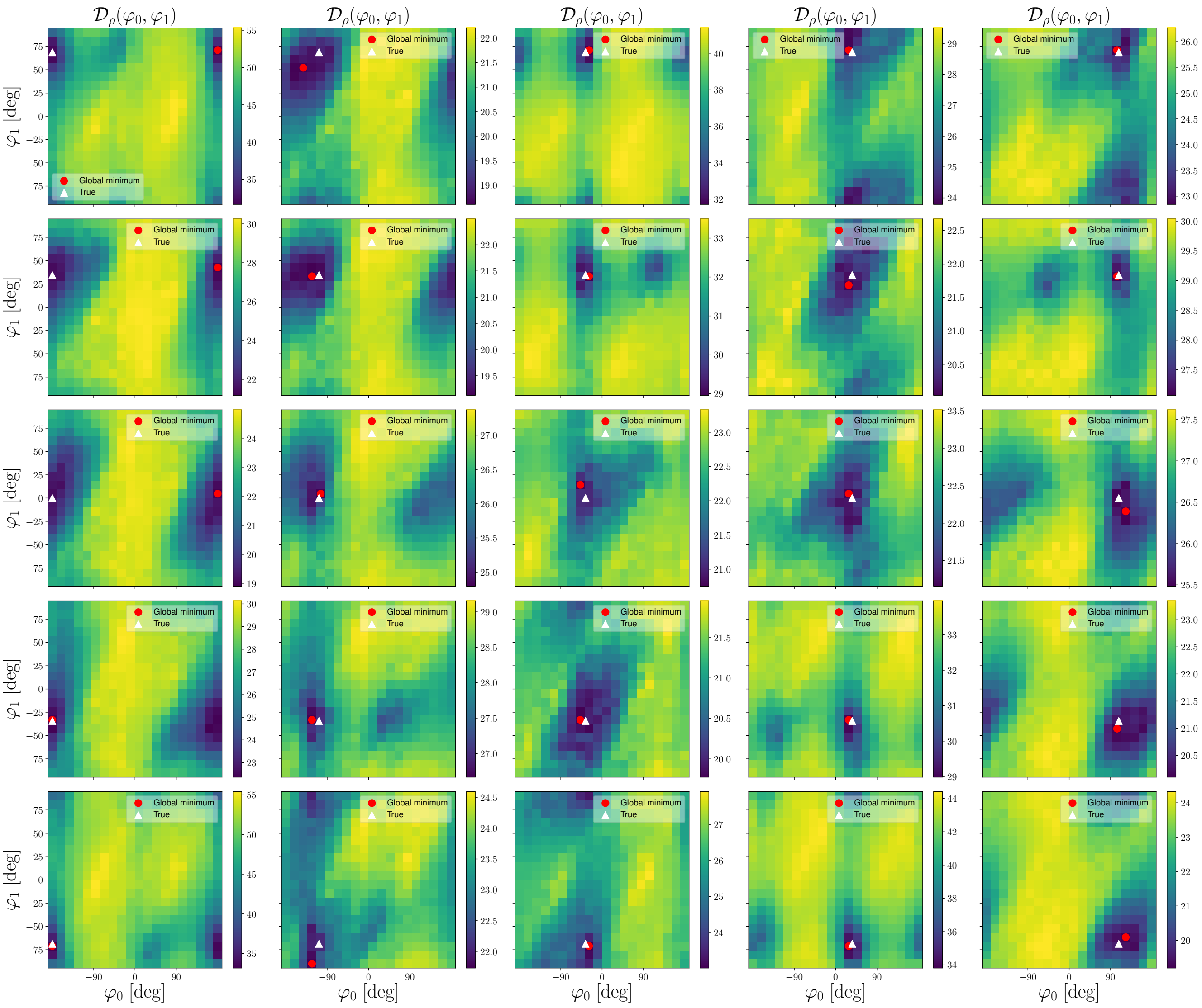

Figure S2: A 2D data-fit manifold over possible $\boldsymbol{\Theta} = (\varphi_0, \varphi_1)$ for a 5×5 grid of measurements $\mathbf{y} = \boldsymbol{\rho}$ that correspond to different $\boldsymbol{\Theta}_{\text{true}}$. The global minima track the ground-truth. Note that due to periodicity the manifolds wrap around in both the horizontal and vertical axes.

in a setting of extremely sparse measurements as is illustrated by the recoveries from synthetic EHT2017 measurements.

S5. Interferometric Measurements

In order to solve the estimation problem posed by Eq. (26) we rely on block coordinate descent and derive a joint estimation approach for the static envelope $\mathbf{I}$ and dynamic parameters $\boldsymbol{\Theta}$ (Eqs. 27–28). In this section we extend the derivations provided in Sec. 4.2.3.

S5.1. Dynamic Parameter Estimation & Linearization

To efficiently solve the dynamic parameter estimation (Eq. 28) we linearize the measurement model (Eq. 25):

$$\mathcal{M}\left[V\left(\mathbf{x}\right)\right] = \mathcal{S}\circ\mathcal{F}\left[I\left(\boldsymbol{x}\right)e^{\hat{\rho}(\boldsymbol{x})}\right] \simeq \mathcal{S}\circ\mathcal{F}[I\left(\boldsymbol{x}\right)] + \mathcal{S}\circ\mathcal{F}[I\left(\boldsymbol{x}\right)\hat{\rho}\left(\boldsymbol{x}\right)]\,. \tag{S8}$$

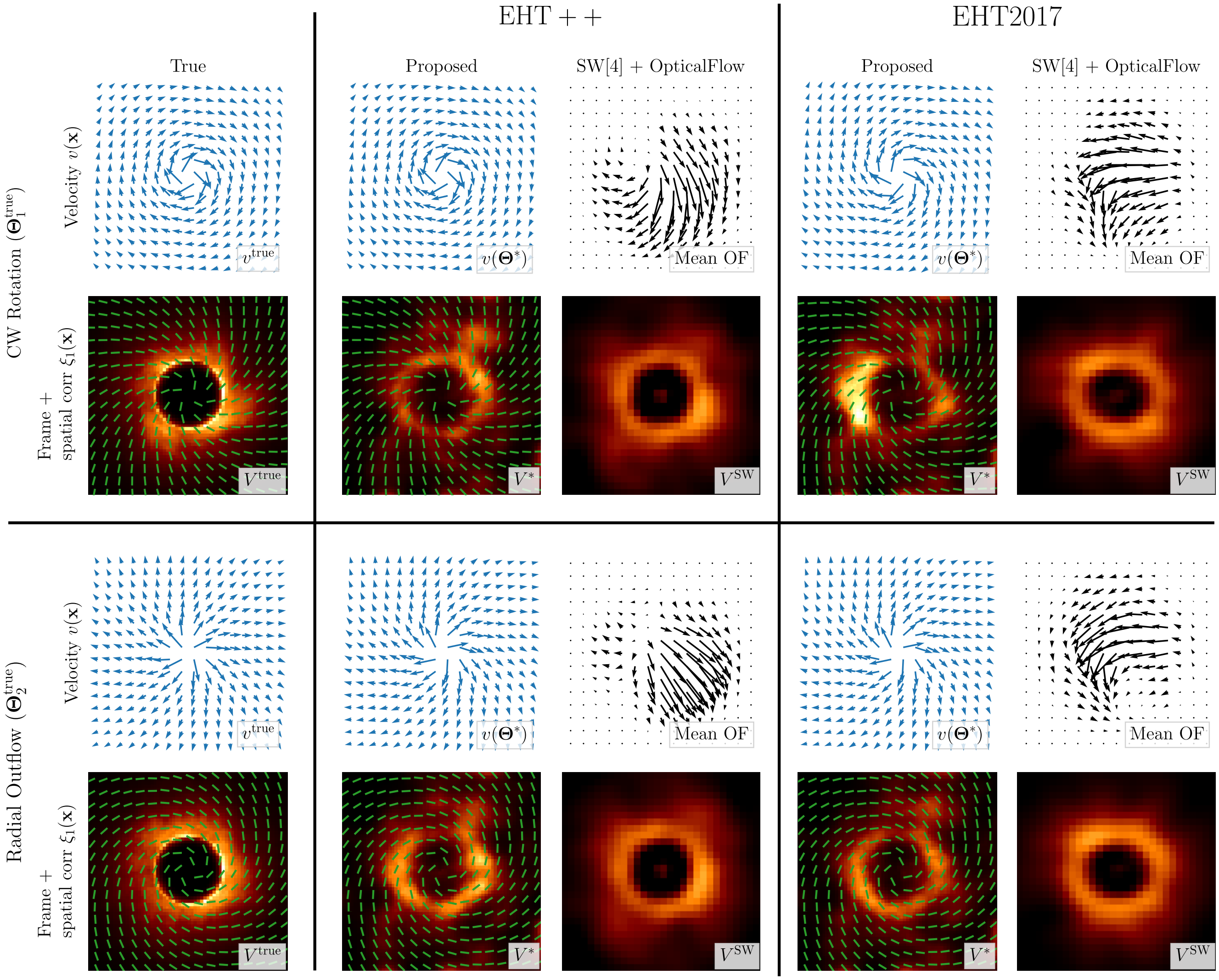

Figure S3: Comparison of the proposed (stochastic model-based) approach with StarWarps (SW) [1] for EHT++ and EHT2017 measurements and two underlying dynamic evolutions generated with $\mathbf{\Theta}_1^{\text{true}}, \mathbf{\Theta}_2^{\text{true}}$. The top two rows correspond to CW rotation and the bottom two rows correspond to radial outflow. The left most column shows the true underlying dynamics where blue arrows describe the velocity field $\boldsymbol{v}$ and green ticks (overlaying the image frames) describe $\boldsymbol{\xi}_1$. The output of SW is an estimated full length video, from which we extract the mean OpticalFlow (OF) field [2] as a proxy of the underlying velocity field. Our proposed model fitting approach is better able to recover the stochastic evolution of the underlying flow field even from very sparse data of EHT2017.

The low dimensional random field $\hat{\rho}$ is given by a series expansion of the SPDE modes (Eq. 14)

$$\hat{\rho}\left(\mathbf{x}\right) = \sum_{k=0}^{K-1} c_k \sigma_k u_k\left(\mathbf{x}\right). \tag{S9}$$

Using the series representation, Eq. (S8) can be written as

$$\mathcal{M}\left[V\left(\mathbf{x}\right)\right] \simeq \mathcal{S}\circ\mathcal{F}[I\left(\boldsymbol{x}\right)] + \sum_{k=1}^{K} c_k \sigma_k \mathcal{S}\circ\mathcal{F}\big[I\left(\boldsymbol{x}\right) u_k\left(\mathbf{x}\right)\big]. \tag{S10}$$

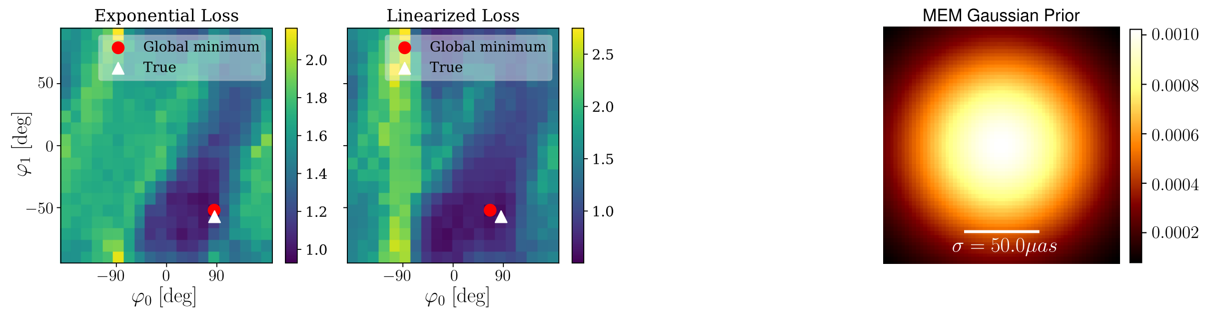

(a) Linearization comparison

(b) MEM Regularization

Figure S4: (a) Loss comparison, using EHT2025, of the linearized and exponential models. While the loss degradation is minimal, the computational gain is significant. Computing the loss with the exponential model (left) took ~6 hours whereas the linearized loss (right) took only ~5 minutes. (b) Prior image $g\left(\boldsymbol{x}\right)$ of a Gaussian with standard deviation of 50μas used for MEM regularization (Eq. S15) of static image reconstruction (Eq. S14).

The sum in Eq. (S11) can be written using matrix multiplication

$$\sum_{k=1}^{K} c_k \sigma_k \mathcal{S} \circ \mathcal{F}\big[I\left(\boldsymbol{x}\right) u_k\left(\mathbf{x}\right)\big] = \mathbf{Z}_{\boldsymbol{\Theta},\mathbf{I}} \boldsymbol{\Sigma}_{\boldsymbol{\Theta}} \mathbf{c}, \tag{S11}$$

where we define $\mathbf{Z}_{\boldsymbol{\Theta},\mathbf{I}}$ as a matrix whose kth column is the sampled Fourier transform of mode u_k: $\mathcal{S} \circ \mathcal{F}\big[I\left(\boldsymbol{x}\right) u_k\left(\mathbf{x}\right)\big]$. Note that $\mathbf{Z}_{\boldsymbol{\Theta},\mathbf{I}}$ depends on both the static envelope and dynamic parameters. By using the linearization (Eqs. S10–S11) to approximate the measurement model (Eq. 25) we derive a *linear* convex minimization problem for inference from visibility measurements

$$\hat{\mathcal{D}}_\nu(\mathbf{y}, \mathbf{I}^*, \boldsymbol{\Theta}) = \min_{\mathbf{c}} \left\|\tilde{\mathbf{y}} - \mathbf{Z}_{\boldsymbol{\Theta},\mathbf{I}^*} \boldsymbol{\Sigma}_{\boldsymbol{\Theta}} \mathbf{c}\right\|^2_{\boldsymbol{\Sigma}_{\mathrm{y}}} + \|\mathbf{c}\|^2. \tag{S12}$$

Here

$$\tilde{\mathbf{y}} = \mathbf{y} - \mathcal{S} \circ \mathcal{F}[I^*\left(\boldsymbol{x}\right)] \tag{S13}$$

can be intuitively interpreted as the *current estimate* of the dynamic portion of the visibility measurements (current estimate since it depends on $\mathbf{I}^*$). The motivation for linearizing the image formation model is efficiency. The validity of the approximation depends on the scaling factor γ (Eq. 1). For the values used in our simulations, $\gamma \approx 2.0$, this yields a significant run-time improvement with minimal degradation. In Fig. S4a) we compare two losses resulting from the linearized and exponential model. While the linearized loss appears less smooth and with a wider minimum around the true value, the computational gain is $\sim$ 2 orders of magnitude

S5.2. Static Image Reconstruction

In Secs. 4.2.1–4.2.2 we formulated inverse problems for direct estimation of model parameters from video pixels. In this case static image effects on the video can be easily subtracted. In contrast, when recovering dynamic parameters from visibility measurements, we jointly estimate the underlying static image $\mathbf{I}$. To estimate the static image, we keep the dynamic parameters fixed and solve the following minimization

$$\mathbf{I}^* = \min_{\mathbf{I}} \left\|\mathbf{y} - \mathcal{S} \circ \mathcal{F}\left[I\left(\boldsymbol{x}\right) e^{\hat{\rho}^*\left(\boldsymbol{x}\right)}\right]\right\|^2_{\boldsymbol{\Sigma}_{\mathrm{y}}} + \alpha \mathcal{R}(\mathbf{I}). \tag{S14}$$

Here α is a weight parameter. In our numerical simulations we used $\alpha = 1.0$ and Maximum Entropy Method (MEM) regularization [4]:

$$\mathcal{R}(\mathbf{I}) = \int_{\boldsymbol{x}} I\left(\boldsymbol{x}\right) \log\left(\frac{I\left(\boldsymbol{x}\right)}{g\left(\boldsymbol{x}\right)}\right) \mathrm{d}\boldsymbol{x}. \tag{S15}$$

Here $g\left(\boldsymbol{x}\right)$ is a prior image. In our reconstructions we used a Gaussian [9] with standard deviation of 50μas (Fig. S4b).

Telescopes Sites				
Arrays	Site	Lat. (°)	Lon. (°)	Alt. (m)
EHT2017 EHT++ ngEHT	ALMA	-23.03	-67.75	5070
	APEX	-23.01	-67.76	5100
	PV	37.07	-3.39	2920
	JCMT	19.82	-155.48	4120
	LMT	18.98	-97.31	4600
	SMA	19.82	-155.48	4110
	SMT	32.70	-109.89	3160
	SPT	-90.00	45.00	2820
EHT++ ngEHT	BAJA	31	-115	2500
	HAY	43	-71	0
	PIKES	39	-105	4000
	KP	31.57	-111.36	1900
	GAM	23.23	16.1	2300
	GLT	72.3	-38.3	3200
EHT++	PDB	44.38	5.54	2620
	CARMA	37.16	-118	2170
	KAUAI	21.55	-159.3	3000
	KEN	-0.1	37.18	5000
	BOL	-16.21	-68.07	5270
	VLT	-24.37	-70.24	2630
	DRAK	-29.28	29.16	3480
ngEHT	BAR	38	-118	2250
	CAT	-41	-71	2000
	CNI	29	-18	2000
	GARS	-63	-58	0
	NZ	-44	171	2000
	OVRO	37	-118	1000
	SGO	-33	-70	3500
	CAS	-55	-68	500
	LLA	-24	-66	4500

Table 1: Existing and candidate sites for an expanded EHT array. The Array column indicates which array configurations contain the sites, for example, all three array configurations (EHT2017, EHT++, ngEHT) contain the existing 8 telescopes.

S5.3. Effect of Sparse Measurements

We analyze the recovery results of the static envelope image and dynamic parameters for increasingly sparse measurements. The top row in Fig. S5 shows the underlying ground truth parameters, a single video frame, and the extracted mean OpticalFlow (OF). The second row shows a reconstruction directly form video pixels. This reconstruction is an upper bound of what we can expect to get from VLBI measurements. We synthesize observation for the next generation EHT [8] (ngEHT) which includes candidate sites for an expanded EHT array - (in total ngEHT has 23 telescopes). EHT++ contains an expanded telescope configuration with 21 telescopes and EHT2017 has the existing 8 telescopes used in the 2017 campaign (see Table 1 for telescope configurations and locations). From top to bottom, Fig. S5 demonstrates the effects of increasingly sparse measurements on the reconstruction quality. Despite errors in recovered envelopes, the dynamic parameter estimation is close to the true underlying parameters. On the right most column Fig. S5 shows the mean OpticalFlow (OF) extracted from movies synthesized with the recovered envelope and dynamic parameters. The general direction of the mean OF field is clockwise (CW) rotation, however, since it is extracted from video pixels it is sensitive to errors in the recovered envelope. A single frame from the synthesized movies is displayed on the second right column.

S6. GRMHD Recovery

In Sec. 5.2 we demonstrate our approach in a more realistic setting, using physics-based video simulations of black hole accretion. We showcase a recovery based on a forward model of General Relativistic Magneto Hydrodynamics (GRMHD) [7] which generated with a spin parameter of $+0.5$. In Fig. S6 we show additional GRMHD recovery where the video was generated with an underlying spin parameter of 0.0. In this case, as shown by the video frame (left column of Fig. S6), the

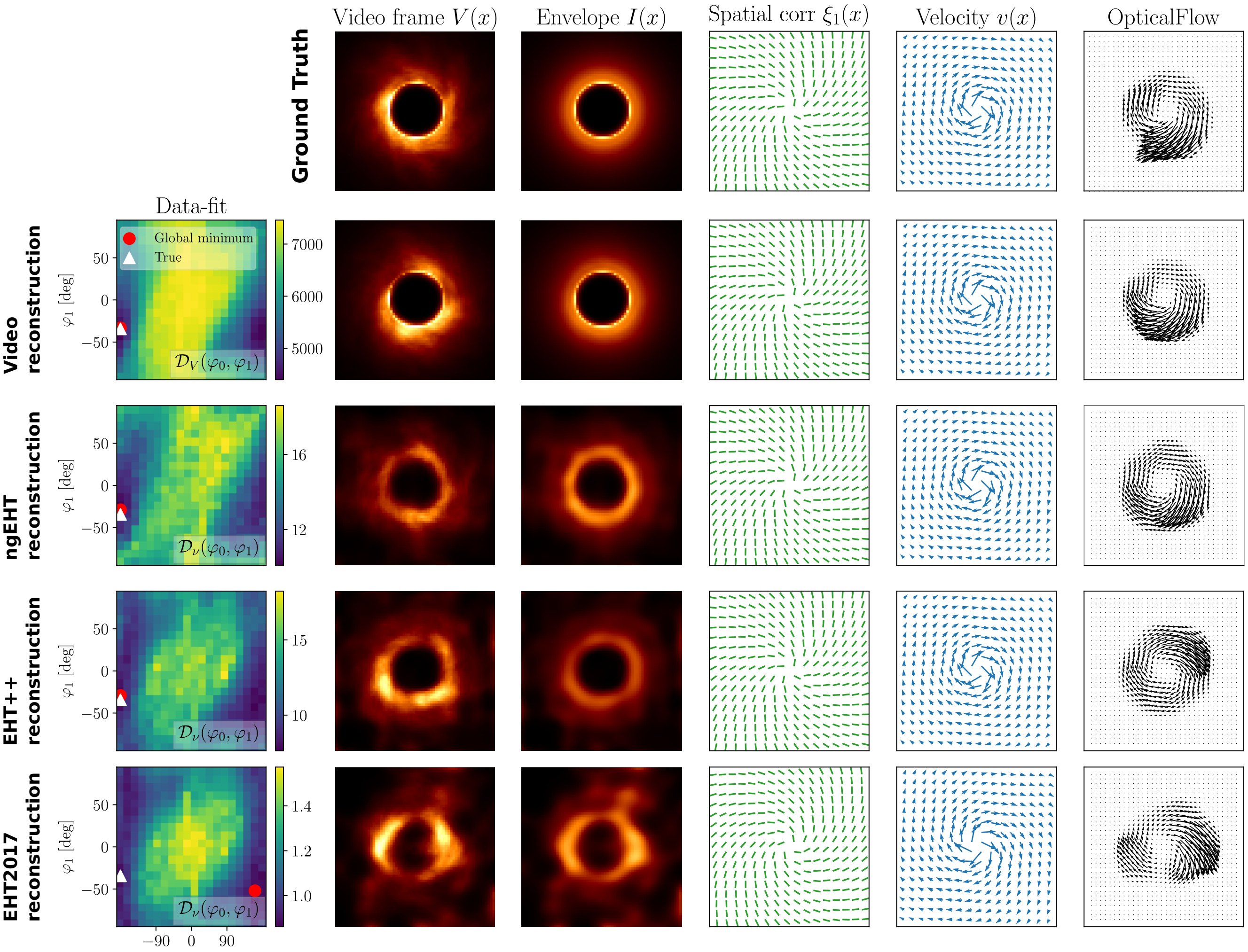

Figure S5: This figure illustrates the effects of sparse measurements on the reconstruction. The top row shows the underlying ground truth parameters and video frame. From top to bottom the measurements used for reconstruction are increasingly sparse. Despite errors in recovered envelopes, the dynamic parameter estimation is close to the true underlying parameters. As measurements become very sparse (EHT2017) the navy-blue region surrounding the global minimum become wider. This is indicative of higher uncertainty in the recovered parameters. The right column shows the mean OpticalFlow (OF) extracted from movies synthesized with the recovered envelope and dynamic parameters. The general direction of the mean OF field is clockwise (CW) rotation, however, since it is extracted from video pixels it is sensitive to errors in the recovered envelope. A single frame from the synthesized movies is displayed on the second right column.

spatial correlation pattern is oriented more radially compared to the $+0.5$ case (shown in the main text Fig. 8).

While we do not have access to ground-truth parameters for GRMHD movies, we can compare the recovery obtained from VLBI measurements to the recovery obtained directly from the GRMHD video, as formulated in Sec. 4.2.2. Recall that we expect the pre-processing step of Eq. (24) to yield a video with similar statistics to the sampled GRFs. Moreover, the 2D loss manifold recovered directly from the pre-processed video is an upper bound of what we can expect to achieve from sparse EHT measurements. Figure S6 shows the recovered envelope and loss manifolds for video data, as well as EHT++ and EHT2017 measurements. In all three cases we estimate a clockwise (CW) rotational field. The loss manifolds for the EHT based recoveries resemble the loss from the video data, with global minima (red dot) around $\varphi_1 = -40°$

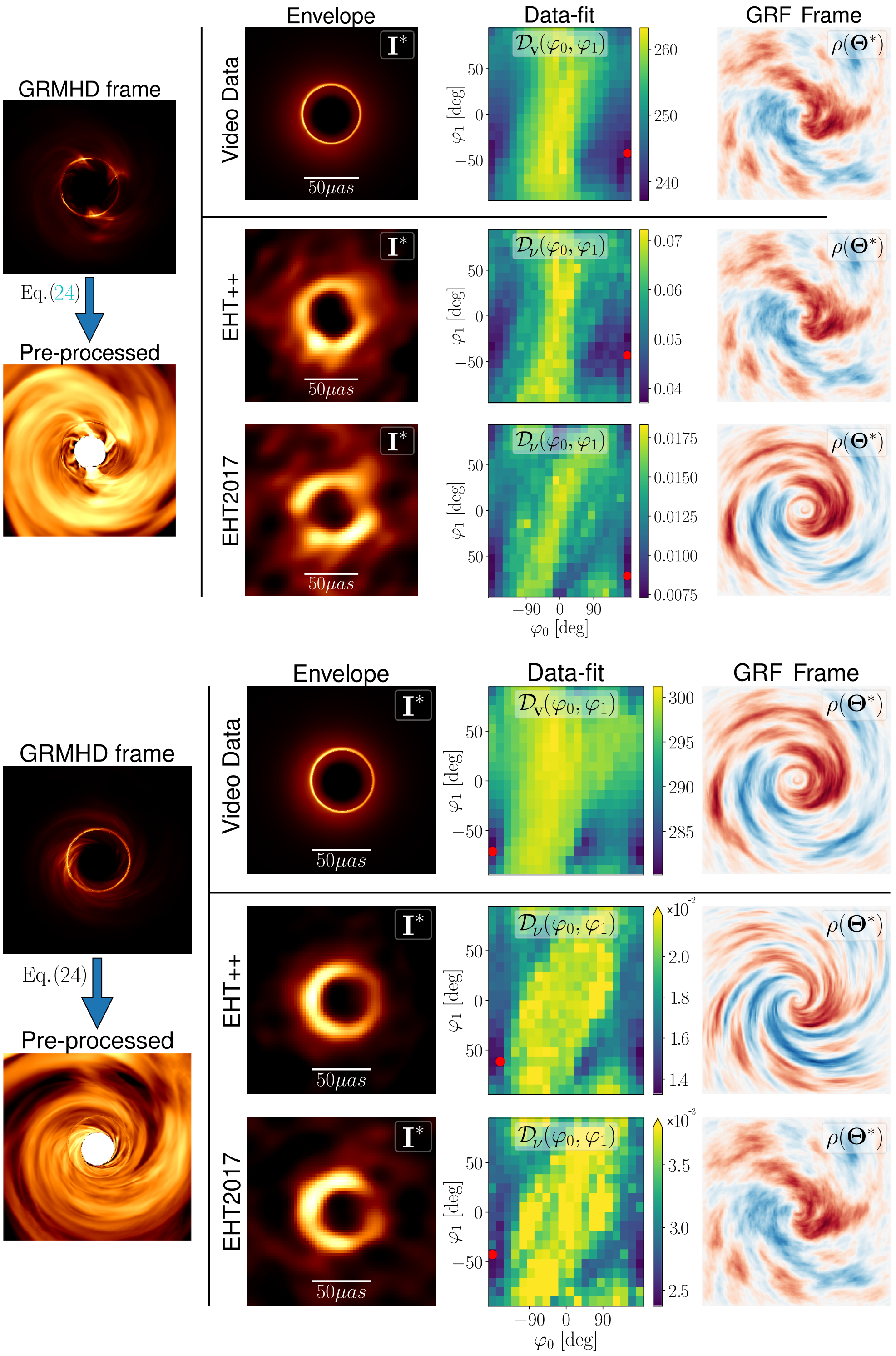

Figure S6: Recovery of the envelope and dynamic parameters of a realistic black hole simulation. The bottom half of the figure shows the result given in the main text (Fig. 8) for comparison. The top half shows an example of a different GRMHD movie with correlations that extend more radially compared to the bottom movie. Reconstruction results are ordered video reconstruction [top] to EHT++ measurements [center], and EHT2017 measurements [bottom]. The left column shows a frame from the GRMHD video and its preprocessed dynamic component (Eq. 24). The right column shows a frame from a GRF sampled with the identified parameters $\mathbf{\Theta}^*$.

References

[1] Katherine L Bouman, Michael D Johnson, Adrian V Dalca, Andrew A Chael, Freek Roelofs, Sheperd S Doeleman, and William T Freeman. Reconstructing video of time-varying sources from radio interferometric measurements. *IEEE Transactions on Computational Imaging*, 4(4):512–527, 2018.

[2] Gunnar Farnebäck. Two-frame motion estimation based on polynomial expansion. In *Scandinavian conference on Image analysis*, pages 363–370. Springer, 2003.

[3] Geir-Arne Fuglstad, Finn Lindgren, Daniel Simpson, and Håvard Rue. Exploring a new class of non-stationary spatial gaussian random fields with varying local anisotropy. *Statistica Sinica*, pages 115–133, 2015.

[4] Stephen F Gull and John Skilling. Maximum entropy method in image processing. In *IEE Proceedings F (Communications, Radar and Signal Processing)*, volume 131, pages 646–659. IET, 1984.

[5] Daeyoung Lee and Charles F Gammie. Disks as inhomogeneous, anisotropic gaussian random fields. *The Astrophysical Journal*, 906(1):39, 2021.

[6] Finn Lindgren, Håvard Rue, and Johan Lindström. An explicit link between gaussian fields and gaussian markov random fields: the stochastic partial differential equation approach. *Journal of the Royal Statistical Society: Series B (Statistical Methodology)*, 73(4):423–498, 2011.

[7] Oliver Porth, Koushik Chatterjee, Ramesh Narayan, Charles F Gammie, Yosuke Mizuno, Peter Anninos, John G Baker, Matteo Bugli, Chi-kwan Chan, Jordy Davelaar, et al. The event horizon general relativistic magnetohydrodynamic code comparison project. *The Astrophysical Journal Supplement Series*, 243(2):26, 2019.

[8] Alexander W Raymond, Daniel Palumbo, Scott N Paine, Lindy Blackburn, Rodrigo Córdova Rosado, Sheperd S Doeleman, Joseph R Farah, Michael D Johnson, Freek Roelofs, Remo PJ Tilanus, et al. Evaluation of new submillimeter vlbi sites for the event horizon telescope. *The Astrophysical Journal Supplement Series*, 253(1):5, 2021.

[9] The Event Horizon Telescope Collaboration. First M87 Event Horizon Telescope Results. IV. Imaging the central supermassive black hole. *The Astrophysical Journal Letters*, 875(1):L4, 2019.

[10] Peter Whittle. On stationary processes in the plane. *Biometrika*, pages 434–449, 1954.